POLITECNICO DI TORINO
Repository ISTITUZIONALE

High-reliability data processing and calculation of microstructural parameters in hydroxyapatite scaffolds produced by vat photopolymerization

Original
High-reliability data processing and calculation of microstructural parameters in hydroxyapatite scaffolds produced by vat photopolymerization / Schiavi, A.; Fiume, E.; Orlygsson, G.; Schwentenwein, M.; Verne', E.; Baino, F.. - In: JOURNAL OF THE EUROPEAN CERAMIC SOCIETY. - ISSN 0955-2219. - ELETTRONICO. - 42:13(2022), pp. 6206-6212. [10.1016/j.jeurceramsoc.2022.06.022]

Availability:
This version is available at: 11583/2973795 since: 2022-12-13T11:23:25Z

Publisher:
Elsevier Ltd

Published
DOI:10.1016/j.jeurceramsoc.2022.06.022

Terms of use:

This article is made available under terms and conditions as specified in the corresponding bibliographic description in the repository

Publisher copyright
Elsevier postprint/Author's Accepted Manuscript

© 2022. This manuscript version is made available under the CC-BY-NC-ND 4.0 license http://creativecommons.org/licenses/by-nc-nd/4.0/.The final authenticated version is available online at: http://dx.doi.org/10.1016/j.jeurceramsoc.2022.06.022

(Article begins on next page)

08 May 2026

High-reliability data processing and calculation of microstructural parameters in hydroxyapatite scaffolds produced by vat photopolymerization

Alessandro Schiavi[1], Elisa Fiume[2], Gissur Orlygsson[3], Martin Schwentenwein[4], Enrica Verné[2], Francesco Baino[2,*]

[1] National Institute of Metrological Research (INRiM), Applied Metrology and Engineering Division, 10135 Turin, Italy.

[2] Department of Applied Science and Technology (DISAT), Politecnico di Torino, 10129 Turin, Italy

[3] Ice Tec, 112 Reykjavik, Iceland.

[4] Lithoz GmbH, Vienna, Austria

Abstract

The accurate determination of mass transport and microstructural properties within highly-porous trabecular bone specimens and substitutes still represents a challenge due to the complex arrangement in the three-dimensional space, where adjacent pores can be hardly identified due to the open-cell disordered structure resulting from the reciprocal alternation of struts and voids.

In the present study, the complete set of mass transport properties of hydroxyapatite (HA) scaffolds produced by digital light processing (DLP)-based vat photopolymerization was determined by applying the recent Ergun-Wu resistance model. Input data include the intrinsic permeability of the scaffolds, obtained by acoustic experimental measurements, and the equivalent pore diameter, calculated as a function of total porosity and average trabecular size from accurate micro-computed tomography (μ-CT) scans.

The results, corroborated by an accurate and robust statistical analysis, were compared with previous literature data and confirmed a feasible and concrete application of DLP-derived HA scaffolds in clinical practice.

Keywords: Hydroxyapatite; Scaffold; Additive manufacturing; Permeability; Porosity.

1. Introduction

Bone is a dynamic and highly adaptive tissue characterized by a well-organized hierarchical structure from the nano- to the macro-scale. At each level of its organization, bone exhibits peculiar physical and mechanical properties which can substantially vary according to the composition and the structural organization of the tissue itself **[1,2]**.

At the macro-scale, bone is conventionally classified into cortical and trabecular bone, according to the level of metabolic activity, the mechanical response, the density of the tissue and, consequently, its mass transport properties **[3]**.

For this reason, trabecular and cortical bones are properly distributed in the skeleton to carry out specific functions: while the high density confers good mechanical resistance to cortical bone under compressive, torsional and tensile stresses, the high porosity level observed in the open-cell architecture of trabecular bone is key for tissue vascularization and facilitates cell migration, nutrient/oxygen supply and elimination of metabolic wastes **[1, 4-6]**.

Over the last decades, great attention was addressed to the development of bone substitutes with three-dimensional (3D) trabecular-like structure. In fact, compared to cortical bone, the trabecular one is more prone to evolve into pathological states and, consequently, more frequently needs therapeutic actions. Most of research in the bone tissue engineering field aims at optimizing osseous substitutes in terms of morphology, mechanical and mass transport properties, and usually refers to the physiological ranges reported for healthy trabecular bone as target values **[7].**

In trabecular bone, the 3D architecture is articulated as a random-distributed network alternating rod-like and plate-like structures, with a trabecular thickness ranging from 200 to 400 μm **[8-11]** and interconnected trabecular voids within 200-300 μm **[12]**, which results in a macro-porosity varying in a wide range (from 40 to 95 vol.% **[13]**), depending on the skeletal site.

While the interconnected voids permit free flow of fluid inside the network, a percentage of dead-end pores, tortuous pores and narrow throats within the structure as well as closed isolated pores, weaken the free flow of fluid or prevent it at all **[14,15]**.

In order to obtain a realistic estimate of the actual biological performance of a scaffold mimicking the trabecular bone architecture in terms of cell attachment, penetration depth and vascularization, it is thus necessary to accurately assess both the microstructural properties, i.e. the morphological

features of void interconnection, and the mass transport properties, i.e. the effective allowed fluid flow.

Intrinsic permeability is a key parameter to quantify the relation between the transport properties, in terms of actual admitted flow-rate of a viscous fluid through the porous resistive material, and the microstructural properties of the material itself **[16]**.

In a previous study, the tomographic reconstruction of an open-cell polymeric foam was used as an input file to a digital light processing (DLP)-based vat photopolymerization system to produce hydroxyapatite (HA) scaffolds with 3D pore-strut architecture and mechanical properties comparable to human cancellous bone **[17]**.

However, a preliminary evaluation of scaffold macro-porosity by scanning electron microscopy (SEM) revealed some criticisms in distinguishing adjacent pores within the fibrous architecture and, as a consequence, it was possible only to qualitatively determine the average equivalent pore diameter of the analyzed scaffolds, which was found to vary in a very wide range, approximately from 100 to 800 μm **[17]**.

In the present study, this limitation was addressed by calculating the scaffold mean equivalent pore diameter as function of the mean trabecular diameter, which was univocally and accurately assessed by micro-computed tomography (μ-CT). These values, together with experimental intrinsic Darcian permeability, were used as input data to the recent Ergun-Wu resistance model in order to determine the complete set of microstructural properties of HA sponge-like scaffolds produced by DLP technology.

2. Materials and methods

2.1 Theoretical background

The present study provides the pore morphology assessment of DLP-derived foam-like hydroxyapatite scaffolds by applying the recent Ergun-Wu resistance model, using the experimental intrinsic Darcian permeability k_D and the equivalent pore diameter d_p as input data. In fact, the Darcian permeability k_D can be related to the effective porosity ε within the scaffold by **Equation 1 [18, 19]**:

$$k_D = \frac{\varphi^2 d_p^2 \varepsilon^3}{72\tau(1-\varepsilon)^2} \quad (1)$$

where φ is the pore sphericity, d_p is the equivalent pore diameter, ε is the effective porosity and τ is the pore tortuosity.

The pore sphericity φ is a numerical quantity representing the degree to which a pore shape is close to a perfect sphere, ranging from 1 (perfect sphere) to 0 (elongated shape) **[20]**. Namely, the pore sphericity is determined from the ratio of the maximum radius of the sphere inscribed in the pore (of any arbitrary shape) and the minimum radius of the sphere circumscribing the pore. Pore sphericity is determined from μ-CT measurements and computational analysis.

The equivalent pore diameter d_p, assumed as the average characteristic length scale of the internal structure of the scaffold, is calculated from **Equation 2 [21-23]**:

$$d_p = \sqrt{\frac{\varepsilon_0}{1-\varepsilon_0}} \cdot d_f \quad (2)$$

where d_f is the average trabecular diameter, determined from statistical analysis of large data set of μ-CT measurements, and ε_0 is the total porosity, calculated by gravimetric method according to **Equation 3 [24]**:

$$\varepsilon_0 = 1 - \frac{\rho_{bulk}}{\rho_{HA}} \quad (3)$$

where ρ_{bulk} is the bulk density of the scaffold (calculated as the mass-volume ratio) and ρ_{HA} (= 3.156 g/cm^3) **[25]** is assumed to be the theoretical density of HA.

Equation 2 allows estimating the average equivalent pore diameter d_p, within a trabecular-like scaffolds, in the form of Xu-Yu equation **[22]**; this parameter is supposed to represent adequately the actual average equivalent pore-channel diameter of Hagen-Poiseuille law within the complexity of randomly-distributed networks of voids **[26, 27]**, by quantifying a close estimation of the effective "size" of open porosity in the trabecular architecture, regardless of trabeculae arrangement, tangle complexity and discontinuities.

The effective porosity ε is defined as the fractional volume of the pores that actually allow fluid flow within the permeable material, without accounting for voids of dead-end pores and closed pores ε_c, according to **Equation 4 [14]:**

$$\varepsilon = \varepsilon_0 - \varepsilon_c \tag{4}$$

The pore tortuosity τ, defined as the ratio between the length L_s of the scaffold and the actual length L_p of the tortuous pore, i.e. $\tau = L_p/L_s$, can be estimated from the comprehensive Yu and Li geometrical model **[28]** as a function of effective porosity ε only (**Equation 5**):

$$\tau = \frac{1}{2}\left[1 + \frac{1}{2}\sqrt{1-\varepsilon} + \sqrt{1-\varepsilon}\,\frac{\sqrt{\left(\frac{1}{\sqrt{1-\varepsilon}}-1\right)^2+\frac{1}{4}}}{1-\sqrt{1-\varepsilon}}\right] \tag{5}$$

Moreover, as shown by Wu et al. **[29, 30]**, from the effective porosity ε, it is also possible to estimate the pore narrowing ratio β, by **Equation 6**:

$$\beta = \frac{1}{1-\sqrt{1-\varepsilon}} \tag{6}$$

The pore narrowing ratio is a resistive term, correlated to the effects of the contraction and expansion of the pore section, representing the ratio of d_p and d_t, namely $\beta = d_p/d_t$, where d_t is assumed as the average diameter of throats; the magnitude of this morphological parameter affects the overall conductance at the pore-scale, in terms of unexpected abrupt interfacial jumps, pressure bursts and occlusions in mass transport **[31-33]**.

Figure 1 shows a schematic representation of pore morphology as discussed above.

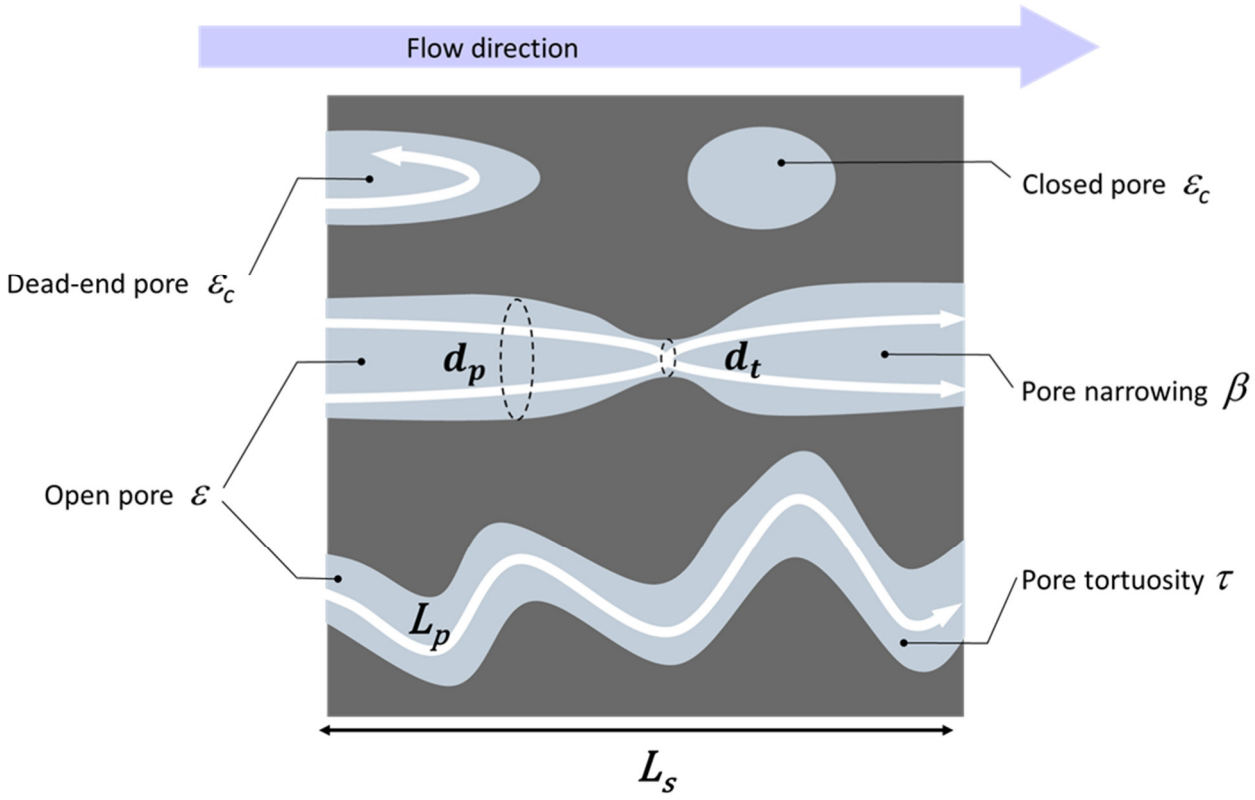

Figure 1. Schematic representation of pore morphology with related quantitative terms.

2.2 Production and preliminary characterization of trabecular-like HA scaffolds

Trabecular-like HA scaffolds were additively manufactured at Lithoz GmbH in Vienna (Austria) and previously characterized in terms of gross morphology, mechanical properties and intrinsic permeability **[17].**

The implemented manufacturing technique was a DLP-based vat photopolymerization process using a computer-aided design (CAD) virtual model of a 45-ppi commercial polyurethane sponge used as input file to the printing system, where sponge 3D reconstruction was obtained by the processing of micro-CT images. After printing, a multistep thermal treatment was applied to remove the binder and sinter the ceramic particles; readers can find additional details about scaffold manufacturing in Ref. **[17].**

The experimental intrinsic Darcian permeability k_D was determined by a microphonic measurement of the pressure wave drop, implemented within a closed volume at very slow flow rate, in order to keep interstitial Reynolds number low enough to avoid turbulent flux within the randomly-distributed networks of voids **[34].**

The physical model used to calculate Darcian permeability values is described by **Equation 7**:

$$k_D = \mu \frac{\omega V_0}{\gamma p_0} \cdot \frac{L}{A} \cdot \left[\frac{\mathrm{mV/Pa}_{cal}}{\mathrm{mV/Pa}_{test}}\right] \quad (7)$$

where μ is the dynamic viscosity of air, ω is the angular frequency of oscillation imposed to the piston, V_0 is the closed volume defined between the piston and the scaffold surface, p_0 is the atmospheric static pressure, γ = 1.4 is the heat capacity ratio, and *L* and *A* are the length and cross-sectional area of the scaffold, respectively. In bracket, the ratio between the calibrated microphone sensitivity, mV/Pa$_{cal}$, and the microphone measurement output mV/Pa$_{test}$, is shown.

Readers can find additional details on the experimental set up used for intrinsic permeability assessment in Refs. **[17, 19]**.

2.3 μ-CT analysis for the determination of the trabecular diameter

Sintered scaffolds underwent X-ray μ-CT analyses to obtain an estimation of the average trabecular diameter d_f and the pore shape factor φ (sphericity).

μ-CT scanning of the hydroxyapatite scaffolds was performed in air on a Phoenix Nanotom S (Waygate Technologies / Baker Hughes Digital Solutions GmbH, Wunstorf, Germany). Projection images were collected using a source voltage of 80 kV and a source current of 120 μA, employing a 0.1 mm thick Cu X-ray filter. A 14.3-fold magnification was used with a voxel size of 3.50 μm. Rotation step size was 0.33°, exposure time 1.5 s and tube mode 0. Mode 0 is one of the four specific modes of the instrument, the so- called power mode with maximum target power 2.7 W. Four images were integrated for each rotation step and one blank image was collected prior to acquisition of these four images. Before reconstruction, a translational motion compensation was used to avoid mismatching between the 0° and the 360° shadow images in case of a slight movement of the sample during the data collection. This compensation was performed in the datos-x reconstruction software provided by the equipment manufacturer. Virtual volumes were reconstructed from the projection images using the datos-x software. The structural features of the scaffolds were determined by using the VGStudio Max 3.3 software (Volume Graphics, Heidelberg, Germany) based on the Cauchy-Crofton approach. Apart from the main software, the add-on modules Coordinate Measurement and Foam/Powder Analysis were used. A virtual cylinder was fitted into the reconstructed scaffold model to avoid effects of the irregular contours of the scaffold and establish a basis for the calculations. The cylinder was extracted as a separate virtual volume and an isovalue-based surface determination procedure was run. The Foam/Powder Analysis module was used to extract foam structure data employing a merge threshold of 5% and a standard

precision procedure. The module allows the segmentation of CT data into separate cells which can be visualized and statistically analysed. In the same way, strut thickness between cells can be quantified and analysed. Data on the diameter of scaffold trabeculae (d_f), or strut thickness, and the pore shape factor φ (sphericity), was extracted.

2.4 Statistical analysis

The geometrical dimensions of 6 scaffolds were determined from 3 repeated micro-caliper measurements of lengths *L* and diameters *D*, with a resolution of 1 μm; the cross-sectional area *A* of the samples perpendicular to the flow direction was calculated accordingly. Results were expressed in terms of average value (μ) ± standard deviation (σ).

Moreover, the geometrical dimensions of the measuring system, the physical properties of airflow, and the output tension data were accurately quantified with related uncertainties.

The average experimental intrinsic Darcian permeability k_D of the scaffolds was determined from 3 different repeated measurements on 6 samples, in order to reliably quantify both repeatability and reproducibility of measurement results.

The uncertainty contributions of physical and mechanical quantities of Darcy's law (**Equation 7**) were accurately investigated by the general rule of random error propagation according to GUM **[35]**, and the experimental results are expressed with a confidence level of 95%.

By considering all variables (geometrical dimensions of sample and measuring system, the physical properties of airflow, and the output tension data) as independent, the uncertainty assessment applied to calculate the expanded uncertainty of each sample U_{sample} is based on **Equation 8**:

$$U_{sample} = k \cdot \sqrt{\sum_{i=1}^{N} \left(\frac{\partial f}{\partial x_i}\right)^2 u^2(x_i)} \tag{8}$$

in which *k* is the coverage factor (namely, *k*=2 provides an interval having a confidence level of approximately 95%), *f* is the **Equation 7,** x_i is the i^{th} independent variable of **Equation 7**, and $u^2(x_i)$ is the standard uncertainty, associated to the independent variable x_i.

3. Results and discussion

The geometrical dimensions of HA scaffolds are collected in **Table 1**. As the reliability of measurements depends on the accuracy of input data, the detailed analysis of associated uncertainties and the related uncertainty propagation of all the variables reported in **Equation 7**, were accurately quantified.

By way of example, **Table 2** reports the detailed uncertainty analysis for a single measurement of intrinsic Darcian permeability k_D of a specific scaffold (Sample #3). The same uncertainty components were also considered for the permeability values of the overall 18 measurements.

Table 1. Geometrical characterization of HA scaffolds (triplicate measurements).

	Height L/mm	Diameter D/mm	Cross-sectional area A/mm^2
	$\mu \pm \sigma$	$\mu \pm \sigma$	$\mu \pm \sigma$
Sample #1	9.90±0.06	4.95±0.23	19.27±1.81
Sample #2	9.78±0.17	5.07±0.29	20.16±2.32
Sample #3	9.91±0.04	4.92±0.15	19.04±1.16
Sample #4	9.66±0.18	4.93±0.10	19.06±0.80
Sample #5	10.05±0.12	5.07±0.07	20.19±0.56
Sample #6	9.98±0.03	5.00±0.04	19.66±0.33

Table 2. Uncertainty analysis, according to GUM rules (**Equation 8**), for a single measurement of intrinsic Darcian permeability related to Sample #3.

Variable x_j	**Value**	**Note**	$u^2(x_j)$	$\partial f/\partial x_i$	$u_c^2(y)$
μ/Pa·s	$1.825\cdot10^{-5}$	tolerance	$3.3\cdot10^{-17}$	$8.0\cdot10^{-5}$	$2.1\cdot10^{-25}$
ω/rad·s^{-1}	0.942	tolerance	$3.3\cdot10^{-7}$	$1.5\cdot10^{-9}$	$8.0\cdot10^{-25}$
V_0/m^3	$2.49\cdot10^{-4}$	tolerance	$2.6\cdot10^{-11}$	$5.9\cdot10^{-6}$	$8.9\cdot10^{-22}$
p_0/Pa	99920	accuracy	$3.3\cdot10^{-1}$	$-1.5\cdot10^{-14}$	$7.1\cdot10^{-29}$
L/m	$9.91\cdot10^{-3}$	tolerance	$3.1\cdot10^{-9}$	$1.5\cdot10^{-7}$	$6.8\cdot10^{-23}$
A/m^2	$1.90\cdot10^{-5}$	tolerance	$2.5\cdot10^{-12}$	$-7.5\cdot10^{-5}$	$1.4\cdot10^{-20}$
$Volt_{cal}$	$4.51\cdot10^{-1}$	accuracy	$3.3\cdot10^{-13}$	$3.2\cdot10^{-9}$	$3.5\cdot10^{-30}$
$Volt_{cal}$		resolution	$7.5\cdot10^{-11}$	$3.2\cdot10^{-9}$	$7.8\cdot10^{-28}$
$Volt_{test}$	$4.85\cdot10^{-3}$	accuracy	$3.3\cdot10^{-13}$	$-3.0\cdot10^{-7}$	$3.0\cdot10^{-26}$

$Volt_{test}$		resolution	$1.1 \cdot 10^{-7}$	$-3.0 \cdot 10^{-7}$	$9.6 \cdot 10^{-21}$
k_D /m²	**$1.46 \cdot 10^{-9}$**		Variance, **u^2**		$2.4 \cdot 10^{-20}$
			Standard uncertainty, **u**		$1.6 \cdot 10^{-10}$
			Confidence level		95%
			Expanded uncertainty, **U_{sample}**		**$0.31 \cdot 10^{-9}$**
			Relative expanded uncertainty		**21.4%**

Referring to the values reported in **Table 2**, it was found that the major individual contributions to the combined standard uncertainty were associated to the geometrical dimensions of the samples, i.e. the cross-sectional area *A* of the sample, and to the accuracy of tension output $Volt_{test}$, since experimental values of $Volt_{test}$ (6 ÷ 4 mV) were close to microphone calibrated sensitivity (0.69 mV/Pa).

Figure 2 shows the overall distribution of experimental results and related uncertainties of the intrinsic Darcian permeability k_D for the 6 scaffolds analyzed.

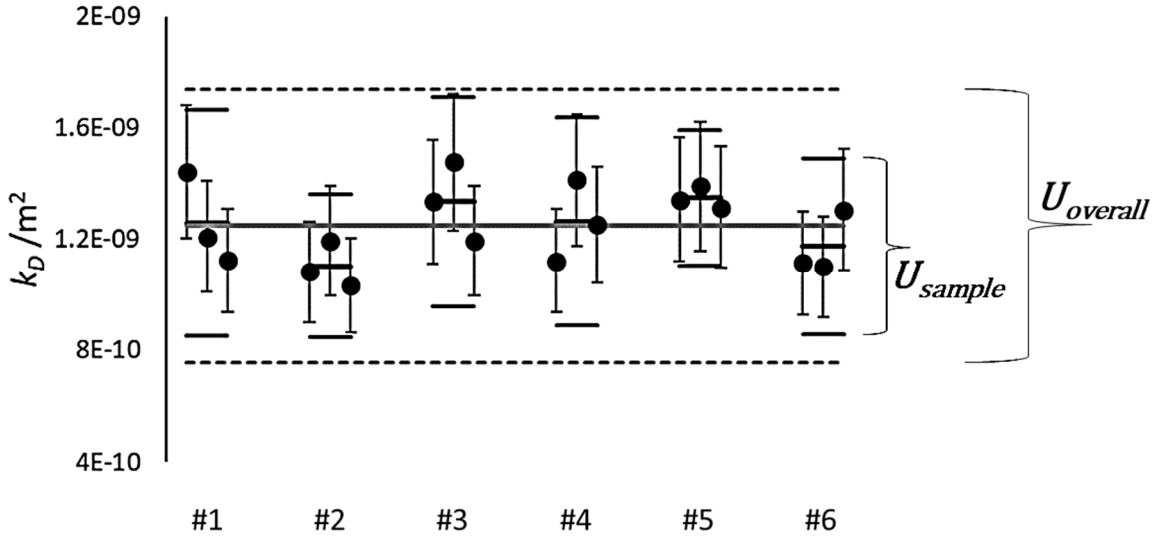

Figure 2. Experimental data distribution: experimental results (•) with individual expanded uncertainties; average of 3 measurements and expanded uncertainties within the same sample (black lines), U_{sample}; total average from 18 measurements (thick gray line) and related overall expanded uncertainty (dotted gray line), $U_{overall}$.

Table 3 collects the overall experimental results of intrinsic Darcian permeability k_D of the 6 scaffolds and related expanded uncertainties.

Table 3. Intrinsic Darcian permeability and expanded uncertainty for HA scaffolds.

	Permeability k/m^2	Standard deviation	Expanded Uncertainty
	$\boldsymbol{k}\cdot 10^{-9}$ /m^2	$\boldsymbol{\sigma}\cdot 10^{-9}$/m^2	$\boldsymbol{U_{sample}}\cdot 10^{-9}$/m^2
Sample #1	1.26	0.17	0.41
Sample #2	1.10	0.08	0.26
Sample #3	1.34	0.14	0.38
Sample #4	1.26	0.15	0.37
Sample #5	1.35	0.04	0.24
Sample #6	1.17	0.12	0.32
Overall value	**1.25**	**0.14**	**0.49**

The overall mean value of Darcian permeability k_D among samples, and the corresponding standard deviation, were 1.25±0.14 $\cdot 10^{-9}$ m^2, with a related overall associated expanded uncertainty of 0.49 $\cdot 10^{-9}$ m^2, respectively.

The overall standard deviation $\sigma_{overall}$ = 0.14$\cdot 10^{-9}$ m^2 was determined from 18 measurements (3 repetitions on 6 samples); the overall expanded uncertainty, $U_{overall}$ = 0.49$\cdot 10^{-9}$ m^2, was evaluated according to the **Equation 9 [35]**:

$$U_{overall} = 2\sqrt{\left(\frac{U_{sample,MAX}}{2}\right)^2 + \sigma_{overall}^2} = 2\sqrt{\left(\frac{0.41}{2}\right)^2 + (0.14)^2} \cong 0.49 \qquad (9)$$

where $U_{sample,MAX}$ is the maximum expanded uncertainty among samples, namely the expanded uncertainty of sample #1.

Therefore, the intrinsic Darcian permeability k_D of the HA scaffolds can be eventually expressed in the range of $0.76 \cdot 10^{-9}$ to $1.74 \cdot 10^{-9}$ m^2, or as $k_D = (1.25 \pm 0.49) \cdot 10^{-9}$ m^2, with a confidence level of 95%.

These results are comparable with the permeability values of human trabecular bone reported in the literature by several authors: for example, Grimm and Williams **[36]** determined the permeability of calcaneus trabecular bone to be in the range of $0.4 \cdot 10^{-9}$ to $11.0 \cdot 10^{-9}$ m^2, while Nauman et al. **[37]** reported values within 1.5-12.1$\cdot 10^{-9}$ m^2 and 0.01-4.7$\cdot 10^{-9}$ m^2 for vertebral bodies and proximal femur, respectively. These studies reveal that, in general, natural bone permeability may vary over a quite broad range depending on the anatomical site.

Previous SEM analyses **[17]** revealed that the DLP-derived HA scaffolds exhibit an open-cell architecture given by the spatial arrangement of spheroidal macro-pores and struts with roughly-circular cross-section (trabeculae). Hence, each scaffold can be interpreted as a 3D fibrous structure where the "filaments" correspond to rod-like HA trabeculae. This physical model, illustrated in **Equation 2,** has already been used for describing natural and synthetic polymeric materials **[23],** but has not been applied to porous bio-ceramics (and porous ceramics in general) so far and is proposed for the first time in the present work.

The diameter of the scaffold trabeculae d_f and the pore shape factor φ (sphericity) were measured by μ-CT analysis (**Figure 3**). The overall number of analyzed diameters was about $7 \cdot 10^8$. Given the huge dataset, it was possible to carry out a highly-reliable statistical analysis. **Figure 3a** and **Figure 3b** show the distribution of trabecular diameters and the distribution of pore sphericity within the trabecular-like architecture, respectively.

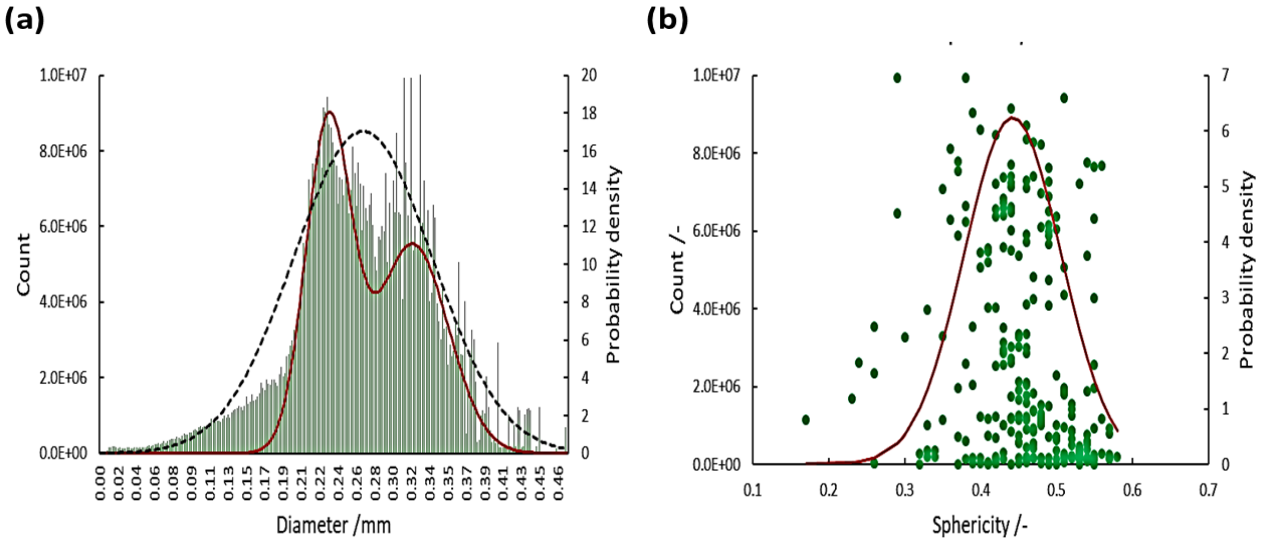

Figure 3. μ-CT experimental data analysis: (a) distribution of trabecular diameters (the red curve is the bimodal distribution, while the dotted curve is the normal distribution); (b) distribution of pore sphericity and the related normal distribution.

Trabecular diameters followed a bimodal distribution instead of a normal one (**Figure 3a**), which can be mainly attributed to the crossing (or overlapping) of the trabeculae. In fact, the measured diameter is greater at the crossing points (intersection regions) of struts as compared to single trabecula (i.e., fiber), as schematically illustrated in **Figure 4**.

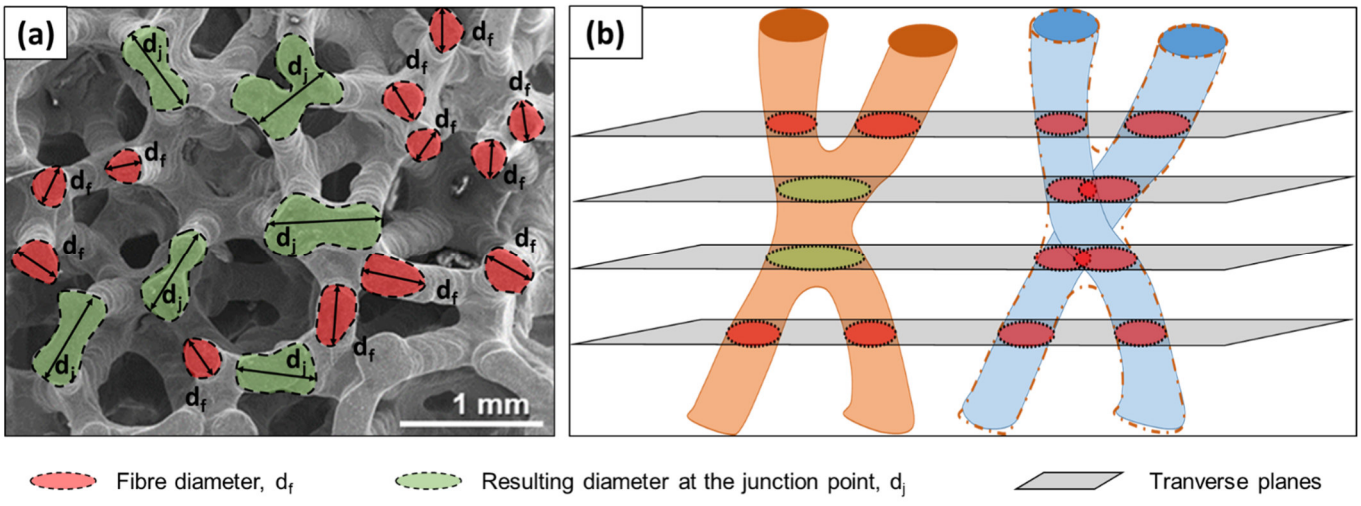

Figure 4. SEM image showing the different cross-sectional areas of scaffold trabeculae (a) and schematic representation of trabecular crossing (b). The trabecular diameter at the junction point (dj) can actually be broken down into the sum of two contributions (d_{f1}+d_{f2}), thus considering the crossing as a trabecular overlapping rather than an interpenetration of fibrous structures.

Therefore, the actual average diameter of trabeculae d_f and the related statistical dispersion are clearly identified from the first peak of the bimodal distribution reported in **Figure 3a**, while the large dispersion of higher values is due to the random crossings and apparent large diameters of the trabecular overlapping. The average diameter of trabeculae is $d_f = 0.231 \pm 0.023$ mm. The histogram of diameters (**Figure 3a**) was built with 0.002 mm width-classes; specifically, ~ $2 \cdot 10^8$ data were collected within the standard deviation of the first peak, namely from 0.208 mm to 0.254 mm. The average pore sphericity is estimated from the related Gaussian dispersion (**Figure 3b**) as $\varphi = 0.442 \pm 0.064$.

The average diameter of the equivalent pore within the trabecular-like structure d_p, was calculated from **Equation 2** along with related expanded uncertainty (**Table 4**); the latter was determined by applying the same rule of **Equation 8.**

Table 4. Uncertainty analysis of the equivalent pore diameter according to GUM rules.

Variable x_j					
Symbol	Value	Note	$u^2(x_j)$	$\partial f/\partial x_i$	$u_c^2(y)$
d_f/mm	0.231	tolerance	$1.3 \cdot 10^{-4}$	1.96	$5.2 \cdot 10^{-4}$
ε_0	0.793	tolerance	$5.0 \cdot 10^{-5}$	1.38	$9.5 \cdot 10^{-5}$
d_p /mm	**0.452**		Variance, **u^2**		$6.1 \cdot 10^{-4}$
			Standard uncertainty, **u**		$2.5 \cdot 10^{-2}$
			Confidence level		95%

Expanded uncertainty, ***U***	**0.049**
Relative expanded uncertainty	**10.8%**

The uncertainty of total porosity is calculated from the standard deviation of the measurements on the six samples, namely $\varepsilon_0 = 0.793 \pm 0.014$.

As a consequence, the average equivalent-pore diameter ranges from 0.403 mm to 0.501 mm, namely $d_p = 0.452 \pm 0.049$ mm, with a confidence level of 95%. This range is suitable for bone tissue engineering applications allowing nutrient/cell perfusion and adequate oxygenation to the implanted scaffold **[24].**

Based on the above-described accurate experimental results, it is possible to determine the effective porosity ε rearranging **Equation 1**, as follows:

$$\frac{72k_D}{\varphi^2 d_p^2} = \frac{\varepsilon^3}{\tau(1-\varepsilon)^2} \tag{13}$$

where the pore tortuosity τ is a function of effective porosity ε only, as shown in **Equation 5**.

The effective porosity of the scaffold can be finally assessed by calculating the zero-values of **Equation 13**, considering only the real solution in the domain $0<\varepsilon<1$ as acceptable. More specifically, the constant term of **Equation 13** is calculated by propagating the related expanded uncertainties of the experimental quantities, in order to obtain the actual range of effective porosity and the derived microstructural properties of the HA scaffolds with a confidence level of 95%. The detailed uncertainty analysis is shown in **Table 5**.

Table 5. Uncertainty analysis related to the constant term in **Equation 5**, according to GUM rules.

Variable x_j					
Symbol	Value	Note	$u^2(x_j)$	$\partial f/\partial x_i$	$u_c^2(y)$

k /m^2	$1.25\cdot10^{-9}$	tolerance	$6.1\cdot10^{-20}$	$1.8\cdot10^{9}$	$2.0\cdot10^{-1}$
φ /–	0.442	tolerance	$1.1\cdot10^{-3}$	-10.17	$1.1\cdot10^{-1}$
d_p /m	$0.452\cdot10^{-3}$	tolerance	$6.1\cdot10^{-10}$	-9947.5	$3.6\cdot10^{-5}$
constant term	**2.2506**		Variance, u^2		$3.7\cdot10^{-1}$
			Standard uncertainty, u		$6.1\cdot10^{-1}$
			Confidence level		95%
			Expanded uncertainty, U		**1.1939**
			Relative expanded uncertainty		**53%**

As a result, the constant term of **Equation 5** ranges between 1.0567 and 3.4445 (i.e., 2.2506$\pm$1.1939) with a confidence level of 95%, and thus the effective porosity ε, calculated from **Equation 13**, ranges from 0.60 to 0.71.

Table 6 collects the ranges of microstructural properties depending on the effective porosity of HA scaffolds investigated in this work. The relevant literature recommends a total porosity above 50 vol.% for tissue engineering scaffolds because this is the lower threshold that is typically exhibited by human cancellous bone **[24]**. This requirement is fulfilled by HA scaffolds as ε is in the range of 60 to 71 vol.%. Higher porosities are typical of diseased states of bone, like osteoarthritic (76 ± 8 vol.%) or osteoporotic bone (78 ± 5 vol.%) **[38]**; therefore, from the viewpoint of effective porosity, DLP-derived scaffolds actually mimic the healthy trabecular bone.

Closed porosity is limited, consistently with natural cancellous bone: in fact, the macropores of trabecular bone are highly open and interconnected and, thus, the total porosity can be considered almost equal to effective porosity **[39]**.

Apart from permeability, whose significance was already discussed in the manuscript, tortuosity and narrowing ratio of pore are other interesting, often ignored parameters providing a measure of the

sinuosity and the narrowing of pores, with great influence on mass/fluid transport and flow propagation and diffusion.

Cancellous bone is commonly modeled as a two-phase porous medium comprising a solid skeleton (struts/fibers) along with macro-voids that, in vivo, are not empty but mainly contain bone marrow and blood. Although tortuosity is known to play an important role in the fluid flow through porous media, it has been seldom considered in the field of bone tissue engineering scaffolds and its contribution has not been fully investigated and understood so far because of the complexity of methods for its assessment. The tortuosity range of DLP-derived HA scaffolds is comparable to the values (1.245-2.154) estimated by Roque et al. **[40]**, who applied a geodesic reconstruction algorithm on 3D μ-CT images from ex vivo radius trabecular bone of 15 individuals. In another study, the same research team calculated the tortuosity on the same dataset by applying the fluid velocity field approach and reported lower values (1.026-1.070) **[41]**. The tortuosity range of HA scaffolds is also comparable to that assessed for bioactive glass foams produced by sponge replica method (1.25-1.50) **[17]**.

A correlation between tortuosity and mechanical properties of cancellous bone was also proposed as trabecular networks from radius bone with low values of tortuosity were found to exhibit a higher strength when compared to the regions with high tortuosity **[42]**.

Recently, Guerreiro et al. **[43]** proposed a method for scaffold selection based on the tortuosity of different 3D geometries having triply periodic minimal surfaces. Although these scaffolds were only virtual models generated by a software, the combination of such computational strategies with additive manufacturing technologies, such as vat photopolymerization, could open new horizons for scaffold optimization and fabrication in the near future.

Moreover, an estimation of the average equivalent-throat diameter, from the narrowing ratio of pore, allows identifying the straining process or mechanical trapping in transportation of comparable-size particles (e.g., drug carrier microspheres, or microorganisms), when the pore throats are too narrow, in drug delivering and cell seeding effectiveness **[44-46]**. The average equivalent-throat diameter in the bone tissue engineering HA scaffolds here investigated, ranges within 0.166 mm and 0.208 mm. The knowledge of this quantity, in biomechanical and biomedical applications, is useful to identify the maximum allowable size of particles admitted in the flow to keep the diffusivity of mass transport constant and effective within the randomly-distributed networks of voids in the trabecular architecture.

Table 6. Summary of the microstructural properties of DLP-derived HA scaffolds.

Microstructural parameter	*Min*	*Max*
Effective porosity ε	0.60	0.71
Closed porosity ε_c	0.08	0.19
Tortuosity τ	1.215	1.319
Narrowing factor β	2.176	2.727
Tortuous pore length L_t */mm*	12.03	13.06
Average throat diameter d_t/mm	0.166	0.208

4. Conclusions

This work tackles the challenge of reliably determining the complete set of microstructural properties of bone tissue engineering HA scaffolds produced by DLP-based vat photopolymerization. The study provides an uncommon merging of reliability analysis for experimental measurements and mathematical modelling built on well-defined physical variables.

Scaffolds were found to have total porosity of 79.3 ± 1.4 vol.% and average equivalent-pore diameter of 0.452 ± 0.049 mm. The Ergun-Wu mathematical model, supported by μ-CT imaging, was implemented to determine the major microstructural parameters of scaffolds, including effective porosity 65.5 ± 5.5 vol.%, pore tortuosity 1.267 ± 0.052, and equivalent-throat diameter of 0.187 ± 0.021 mm, with a confidence level of 95%. This entire set of parameters, being comparable to the typical ones of human trabecular bone, supports the scaffold suitability for tissue engineering applications.

The overall approach proposed in this study can be extended to other kinds of tissue engineering porous scaffolds as well as to other research or industrial fields involving the use of porous ceramics.

References

[1] J.Y. Rho, L. Kuhn-Spearing, P. Zioupos, Mechanical properties and the hierarchical structure of bone, Med. Eng. Phys. 20 (1998), 92-102, https://doi.org/10.1016/S1350-4533(98)00007-1.

[2] X. Wang, S.Xu, S. Zhou et al., Topological design and additive manufacturing of porous metals for bone scaffolds and orthopaedic implants: A review, Biomaterials 83 (2016), 127-141, https://doi.org/10.1016/j.biomaterials.2016.01.012.

[3] J.D. Black, B.J. Tadros, Bone structure: from cortical to calcium, Orthop. Trauma 34 (2020), 113-119, https://doi.org/10.1016/j.mporth.2020.03.002.

[4] E. F. Morgan, G. U. Unnikrisnan, A. I. Hussein, Bone Mechanical Properties in Healthy and Diseased States, Ann. Rev. Biomed. Eng. 20(2018), 119–143, https://doi.org/10.1146/annurev-bioeng-062117-121139.

[5] F. G. Evans, Factors affecting the mechanical properties of bone, Bull. N. Y. Acad. Med. 49 (1973), 751–764.

[6] J. D. Currey, Effects of differences in mineralization on the mechanical properties of bone, Philos. Trans. R. Soc. B, 304 (1984), 509–518.
[7] F. Johannesdottir, M. L. Bouxsein, Bone structure and biomechanics, in: I. Huhtaniemi (Ed.), Encyclopedia of Endocrine Diseases, Elsevier Science, 2018, pp. 19-30, https://doi.org/10.1016/B978-0-12-801238-3.03760-0.
[8] M.I. Fanuscu, T.-L. Chang, Three-dimensional morphometric analysis of human cadaver bone: microstructural data from maxilla and mandible, Clin. Oral Implants Res. 15(2004), 213-218, https://doi.org/10.1111/j.1600-0501.2004.00969.x.
[9] H.-S. Moon, Y.-Y. Won, K.-D. Kim et al., The three-dimensional microstructure of the trabecular bone in the mandible, Surg. Radiol. Anat. 26 (2004), 466-473, https://doi.org/10.1007/s00276-004-0247-x.
[10] X.S. Liu XS, X.H. Zhang, K.K. Sekhon et al., High-resolution peripheral quantitative computed tomography can assess microstructural and mechanical properties of human distal tibial bone, J. Bone. Miner. Res. 25 (2010), 746-756, https://doi.org/10.1359/jbmr.090822.
[11] S. Boutroy, B.V. Rietbergen, E. Sornay-Rendu et al., Finite element analysis based on in vivo HR-pQCT images of the distal radius is associated with wrist fracture in postmenopausal women, J. Bone Miner. Res. 23 (2008), 392-399, https://doi.org/10.1359/jbmr.071108.
[12] T. Doktoret, J. Valach, D. Kytyr et al., Pore size distribution of human trabecular bone-comparison of intrusion measurements with image analysis, 17th international conference Engineering Mechanics, (2011), Svratka, Czech Republic.
[13] L.C. Gerhardt, A.R. Boccaccini, Bioactive Glass and Glass-Ceramic Scaffolds for Bone Tissue Engineering, Materials (Basel) 6 (2010), 3867-3910, https://doi.org/10.3390/ma3073867.
[14] J. Hommel, E. Coltman, H. Class, Porosity–permeability relations for evolving pore space: a review with a focus on (bio-) geochemically altered porous media, Transp. Porous Media 24 (2018), 589-629, https://doi.org/10.1007/s11242-018-1086-2.
[15] A.G. Hunt, M. Sahimi., Flow, transport, and reaction in porous media: Percolation scaling, critical-path analysis, and effective medium approximation, Rev Geophys. 55 (2017), 993-1078, https://doi.org/10.1002/2017RG000558.
[16] M.A.B. Promentilla, S.M. Cortez, R.A.D.C. Papel et al., Evaluation of microstructure and transport properties of deteriorated cementitious materials from their X-ray computed tomography (CT) images, Materials 9 (2016), 388, https://dx.doi.org/10.3390%2Fma9050388.
[17] F. Baino, G. Magnaterra, E.Fiume et al. DLP stereolithography of hydroxyapatite scaffolds with bone-like architecture, permeability and mechanical properties, J. Am. Ceram. Soc. 115 (2022), 1648-1657, https://doi.org/10.1111/jace.17843.
[18] T. C. Kreipke, G. L. Niebur. Anisotropic permeability of trabecular bone and its relationship to fabric and architecture: a computational study, Ann. Biomed. Eng. 45 (2017), 1543-1554, https://doi.org/10.1007/s10439-017-1805-9.
[19] E. Fiume, A. Schiavi, G. Orlygsson et al. Comprehensive assessment of bioactive glass and glass-ceramic scaffold permeability: Experimental measurements by pressure wave drop, modelling and computed tomography-based analysis. Acta Biomater. 119 (2021), 405-418, https://doi.org/10.1016/j.actbio.2020.10.027.

[20] I. Cruz-Matías, D. Ayala, D. Hiller et al. Sphericity and roundness computation for particles using the extreme vertices model, J. Comp. Sci. 30 (2019), 28-40, https://doi.org/10.1016/j.jocs.2018.11.005.

[21] B. Yu, P. Cheng, A fractal permeability model for bi-dispersed porous media, Int. J. Heat Mass Transf. 45 (2002), 2983-2993, https://doi.org/10.1016/S0017-9310(02)00014-5.

[22] P. Xu P, B. Yu, Developing a new form of permeability and Kozeny–Carman constant for homogeneous porous media by means of fractal geometry, Adv. Water Resour 31 (2008), 74-81, https://doi.org/10.1016/j.advwatres.2007.06.003.

[23] A. Schiavi, L. Shtrepi, D. Corona, Effective scale of microstructure of fibrous permeable materials, 25th International Congress on Sound and Vibration-ICSV25 (2018), Hiroshima, Japan.

[24] V. Karageorgiou, D. Kaplan, Porosity of 3D biomaterial scaffolds and osteogenesis, Biomaterials 26 (2005), 5474-5491, https://doi.org/10.1016/j.biomaterials.2005.02.002.

[25] K.A. Hing, K.A., S.M. Best, W. Bonfield, Characterization of porous hydroxyapatite, J. Mater. Sci. Mater. Med. 10 (1999), 135–145, https://doi.org/10.1023/A:1008929305897.

[26] B. Abbar, A. Alem, A. Pantet et al., Experimental investigation on removal of suspended particles from water using flax fibre geotextiles, Env. Technol. 38 (2017), 2964-2978, https://doi.org/10.1080/09593330.2017.1284270.

[27] B. Abbar, A. Alem, A. Pantet et al., Nonwoven flax fibres geotextiles effects on solute heavy metals transport in porous media, Env. Technol. 41 (2020), 2061-2072, https://doi.org/10.1080/09593330.2018.1555284.

[28] B. Yu, J. Li, A geometry model for tortuosity of flow path in porous media, Chin. Phys. Lett. 21 (2004), 1569-1571, http://dx.doi.org/10.1088/0256-307X/21/8/044.

[29] J. Wu, B. Yu, M. Yun, A resistance model for flow through porous media, Transp. Porous Med. 71 (2008), 331-334, http://dx.doi.org/10.1007/s11242-007-9129-0.

[30] J. Wu, D. Hu, W. Li et al., A review on non-darcy flow—forchheimer equation, hydraulic radius model, fractal model and experiment, Fractals 24 (2016), 1630001, https://doi.org/10.1142/S0218348X16300014.

[31] M. Sakai, Y. Sasaki, T. Kaneko et al., Contribution of Pore-Connectivity to Permeation Performance of Silicalite-1 Membrane; Part I, Pore Volume and Effective Pore Size, Membranes 11 (2021), 382, https://doi.org/10.3390/membranes11060382.

[32] P. Agrawal, A. Raoof, O. Iliev et al., Evolution of pore-shape and its impact on pore conductivity during CO2 injection in calcite: Single pore simulations and microfluidic experiments, Adv. Water Resour. 136 (2020), 103480, https://doi.org/10.1016/j.advwatres.2019.103480.

[33] F. Moebius, D. Or., Inertial forces affect fluid front displacement dynamics in a pore-throat network model, Phys. Rev. 90 (2014), 023019, https://doi.org/10.1103/physreve.90.023019.

[34] A. Schiavi, C. Guglielmone, F. Pennella et al., Acoustic method for permeability measurement of tissue-engineering scaffold. Meas. Sci. Technol. 23 (2012), 105702, http://dx.doi.org/10.1088/0957-0233/23/10/.

[35] JCGM 100 2008 Evaluation of Measurement Data — Guide to the Expression of Uncertainty in Measurement (GUM), France: Joint Committee for Guides in Metrology, Sèvres)

[36] M.J. Grimm, J.L. Williams, Measurements of permeability in human calcaneal trabecular bone, J. Biomech. 30 (1997), 743-745, https://doi.org/10.1016/S0021-9290(97)00016-X.

[37] E.A. Nauman, K.E. Fong, T.M. Keaveny. Dependence of Intertrabecular Permeability on Flow Direction and Anatomic Site. Ann. Biomed. Eng. 24 (1999), 517-524, https://doi.org/10.1114/1.195.

[38] D. Porrelli, M. Abrami, P. Pelizzo et al., Trabecular bone porosity and pore size distribution in osteoporotic patients – A low field nuclear magnetic resonance and microcomputed tomography investigation, J. Mech. Behav. Biomed. Mater. 125(2022), 104933, https://doi.org/10.1016/j.jmbbm.2021.104933.

[39] G. Falvo D'Urso Labate, F. Baino, M. Terzini et al., Bone structural similarity score: a multiparametric tool to match properties of biomimetic bone substitutes with their target tissues, J. Appl. Biomater. Funct. Mater. 14 (2016), e277-e289, https://doi.org/10.5301/jabfm.5000283.

[40] W. L. Roque, K.Arcaro, A. Alberich-Bayarri, Mechanical competence of bone: a new parameter to grade trabecular bone fragility from tortuosity and elasticity, IEEE Transactions on Biomedical Engineering 60 (2013), 1363-1370, https://doi.org/10.1109/tbme.2012.2234457.

[41] W. L. Roque, F. G. Wolf, Computing the tortuosity of cancellous bone cavity network through fluid velocity field, XXIV Brazilian Congress on Biomedical Engineering-CBEB 2014, (2014), Uberlândia, MG-Brazil.

[42] W. L. Roque, K. A Uberlândia (MG-Brazil) rcaro, A. Alberich-Bayarri, Tortuosity and elasticity study of distal radius trabecular bone, 7th Iberian Conference on Information Systems and Technologies- CISTI 2012, (2012), Madrid, Spain.

[43] R. Guerreiro, T. Pires, J.M. Guedes et al., On the tortuosity of TPMS scaffolds for tissue engineering, Symmetry 12 (2020), 596, https://doi.org/10.3390/sym12040596.

[44] C.L. Gaol, L. Ganzer, S. Mukherjee et al., Investigation of clogging in porous media induced by microorganisms using a microfluidic application, Environ. Sci.: Water Res. Technol. 7(2021), 441-454, https://doi.org/10.1039/D0EW00766H .

[45] M. Lengyel, N. Kállai-Szabó, V. Antal et al., Microparticles, microspheres, and microcapsules for advanced drug delivery, Sci. Pharm. 87 (2019), 20, https://doi.org/10.3390/scipharm87030020.

[46] N. Waisbord, A. Dehkharghani, J.S. Guasto, Fluidic bacterial diodes rectify magnetotactic cell motility in porous environments, Nature Comm. 12 (2021), 1-9, https://doi.org/10.1038/s41467-021-26235-6.